S.-T. Yau High School Science Award
Research Report

The Team

Name of team member: Advaith Mopuri
School: Mission San Jose High School
City, State/Province, Country: Fremont, California, USA

Name of team member: Maggie Shen
School: Leland High School
City, State/Province, Country: San Jose, California, USA

Name of instructor: Richard French
Job Title: Senior Research Scientist
School/Institution: Space Science Institute
City, State/Province, Country: Boulder, Colorado, USA

Name of instructor: Ryan Maguire
Job Title: Digital Learning Postdoctoral Associate and Instructor, Mathematics
School/Institution: Massachusetts Institute of Technology
City, State/Province, Country: Cambridge, MA, USA

Title of Research Report

Investigating Particle Properties of Saturn's Narrow Rings from Diffraction Reconstructed Profiles Obtained from Cassini Radio Science

Date

24 August 2024

Declaration of Academic Integrity

The participating team declares that the paper submitted is comprised of original research and results obtained under the guidance of the instructor. To the team's best knowledge, the paper does not contain research results, published or not, from a person who is not a team member, except for the content listed in the references and the acknowledgment. If there is any misinformation, we are willing to take all the related responsibilities.

Commitments on Academic Honesty and Integrity

We hereby declare that we

1. are fully committed to the principle of honesty, integrity and fair play throughout the competition.
2. actually perform the research work ourselves and thus truly understand the content of the work.
3. observe the common standard of academic integrity adopted by most journals and degree theses.
4. have declared all the assistance and contribution we have received from any personnel, agency, institution, etc. for the research work.
5. undertake to avoid getting in touch with assessment panel members in a way that may lead to direct or indirect conflict of interest.
6. undertake to avoid any interaction with assessment panel members that would undermine the neutrality of the panel member and fairness of the assessment process.
7. observe the safety regulations of the laboratory(ies) where we conduct the experiment(s), if applicable.
8. observe all rules and regulations of the competition.
9. agree that the decision of YHSA is final in all matters related to the competition.

We understand and agree that failure to honour the above commitments may lead to disqualification from the competition and/or removal of reward, if applicable; that any unethical deeds, if found, will be disclosed to the school principal of team member(s) and relevant parties if deemed necessary; and that the decision of YHSA is final and no appeal will be accepted.

(Signatures of full team below)

X 

Name of team member: Advaith Mopuri

X 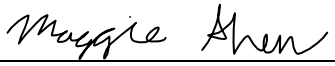

Name of team member: Maggie Shen

X 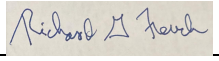

Name of supervising teacher: Richard French

X Ryan Maguire

Name of supervising teacher: Ryan Maguire

Typeset using LaTeX **preprint2** style in AASTeX7.0.1

Investigating Particle Properties of Saturn's Narrow Rings from Diffraction Reconstructed Profiles Obtained from Cassini Radio Science

Advaith Mopuri[1] and Maggie Shen[2]

[1]*Mission San Jose High School, Fremont, CA*
[2]*Leland High School, San Jose, CA*

ABSTRACT

The Cassini mission's Radio Science Subsystem (RSS) conducted occultation observations of the rings by transmitting coherent radiation at wavelengths of 0.94cm (Ka band), 3.6cm (X band), and 13cm (S band) into several Deep Space Networks (DSNs) across the globe. Diffraction effects for each band are primarily caused by particles comparable in size to their wavelengths. As such, comparing the wavelength dependence of optical depth obtained via novel high resolution reconstructions to values predicted by Mie scattering theory allows us to constrain the power-law size distribution of particles in Saturn's rings. Comparing the inferred size distributions for different narrow rings and ring features, we determine that there are significant regional differences in size distributions, which may hold clues about their varying dynamical environments. In particular, we identify differences in particle size distributions between the F ring, the structurally similar Strange ringlet, and the C ring plateaus. Our preliminary results indicate that the F ring properties are different from those of other ring regions, which may be related to the speculated clumpy nature of the F ring itself.

Keywords: Diffraction, Mie scattering, narrow ringlets, particle sizes, radio occultation, Saturn's rings.

ACKNOWLEDGMENTS

We would like to thank Professor Richard French and Dr. Ryan Maguire for proposing this project, providing background knowledge, suggesting ideas, and helping edit this paper. Without their invaluable guidance, support, and expertise, this project would have been impossible. We are also grateful to the MIT PRIMES-USA program for providing this research opportunity. Finally, we would like to thank Professor Matt Hedman, Professor Phil Nicholson, and Dr. Richard Jerousek for offering helpful insights during discussions of this work.

The partition of work in writing the report is as follows: Advaith Mopuri and Maggie Shen jointly wrote Section 1; Maggie wrote Section 2; Advaith wrote Section 3; Advaith wrote Section 4.1 and Maggie wrote Section 4.2 and 4.3; and both Advaith and Maggie jointly wrote Section 5. Professor French and Dr. Maguire assisted in editing and giving feedback on this paper.

Contents

1. INTRODUCTION

Among Saturn's rich and varied system, the F ring and other narrow rings stand apart in their structure and detailed orbits (Murray & French (2018)). First detected in 1979 by the Pioneer 11 spacecraft, then imaged by the two Voyager flybys in the following two years (Colwell et al. (2009)), the F ring was determined to be narrow with a radial width of roughly 50 kilometers, multiple-stranded, and to have a dense core surrounded by a sheet of dust. The eccentric F ring is a complex dynamical environment with a satellite on either side affecting the ring's dynamics: Prometheus, which was found to intermittently shepherd the F ring (Colwell et al. (2009)), and Pandora. A rich set of observations from the Cassini mission from images and from stellar and radio occultations reveals this ring to be a particularly interesting and varied system.

The structure of the F ring has been studied in the past. Cassini images and stellar occultations showed that the F ring is dominated by tiny, micron-sized dust particles, leading researchers to predict that are resupplied from unseen, more massive particles (Murray & French (2018)). Additionally, "jets", thought to be caused by collisions between core material and surrounding objects, and transient clumps observed by the Cassini ISS (Imaging Subsystem) provided more evidence for large particles (Murray & French (2018)). Cuzzi et al. (2024) found that although it is surrounded by dust, the F ring's mass is dominated by a true core less than 1 kilometer in radial width that is structured as a chain of disconnected "arcs" in the same orbit. Furthermore, using star occultations from the Cassini Ultraviolet Imaging Spectrograph (UVIS), Esposito et al. (2008) found evidence for elongated clumps in the F ring known as kittens. Alrebdi & Esposito (2025) refined this description by hypothesizing that the F ring's true core is made up of these kittens, a fraction of which are shepherded by Prometheus.

Though much is known, the F ring still has many mysteries and strange features. It is still unknown how the F ring is confined, and why kittens have formed. Furthermore, Cuzzi et al. (2024) showed that the F ring is only intermittently detected by Cassini, and therefore, is asymmetric. In many respects, the F ring's properties differ substantially from those of other ring regions, making it a valuable target of further investigation.

In this paper, we utilize data from the Cassini Radio Science Subsystem (RSS) to analyze the structure of the F ring and other notable ring features. RSS data from ring occultations performed by Cassini allows us to produce novel high-resolution reconstructions of the optical depth of these ring features at three different wavelenths: 0.94cm (Ka Band), 3.6cm (X Band), and 13cm (S Band). Each band can only detect particles comparable in size to its wavelength, so combining data from all three provides significant constraints on the size distribution of particles in Saturn's rings.

Such size distributions allow us to identify mesoscale structures within a ring, like self-gravity wakes, which are only one or a few orders of magnitude greater than the particles themselves. Furthermore, we can calculate the surface density of the ring or the effective particle size in the ring. Combined with the porosity of particles in the ring, it is also possible to find the mass of the ring itself. Similar analysis has been done on different ring regions; for instance, Jerousek et al. (2020) used this particle size distribution analysis to investigate the C ring and Cassini division. Of particular interest to us is the particle size distribution of narrow ringlets. Due to their elliptical orbits and eccentric nature, these ringlets have various unstable mesoscale structures. We will focus our investigation on two specific narrow ringlets: the F

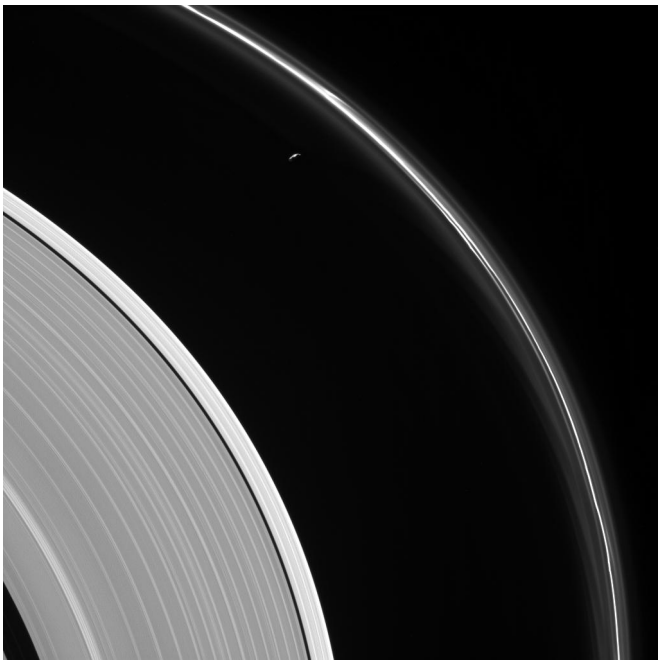

(1a) The F ring and a thin sliver of its shepherding moon, Prometheus. The ring's faint and wispy features seen in this image result from Prometheus' gravitational pull. The image scale is 6 kilometers per pixel.

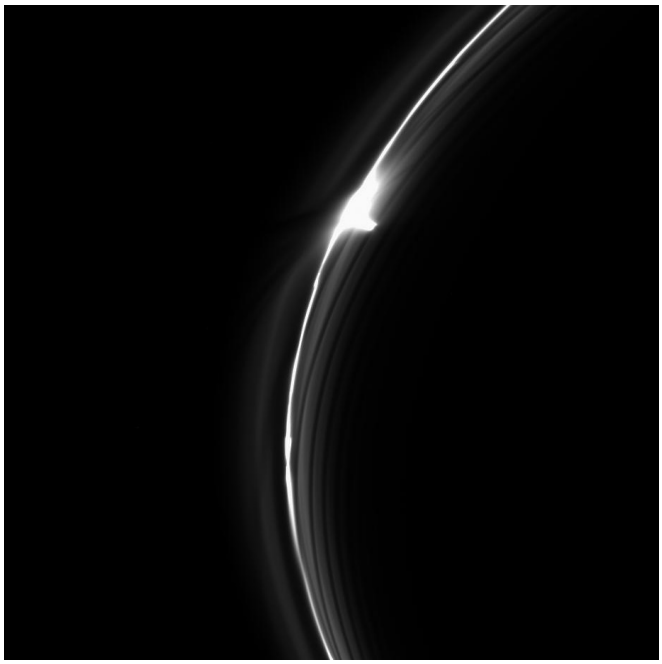

(1b) A variety of features visible in the F ring—a bright clump, "gores" to the right of the bright clump, and a "jet" to the left of the bright clump. The image scale is 2.9 kilometers per pixel.

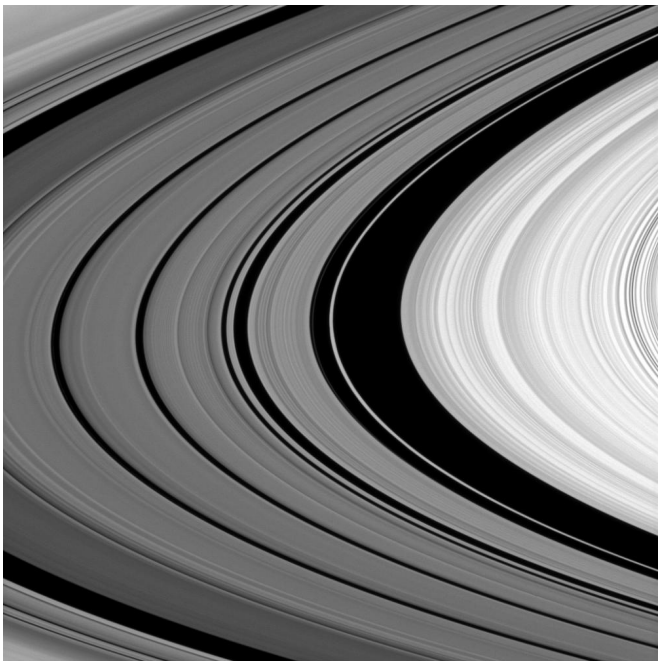

(1c) The Cassini Division occupies most of this image and contains 5 dim bands of ring material. The B ring lies to the right. The largest dark band is the Huygens Gap, within which the Strange ringlet lies. The image scale is 2 kilometers per pixel.

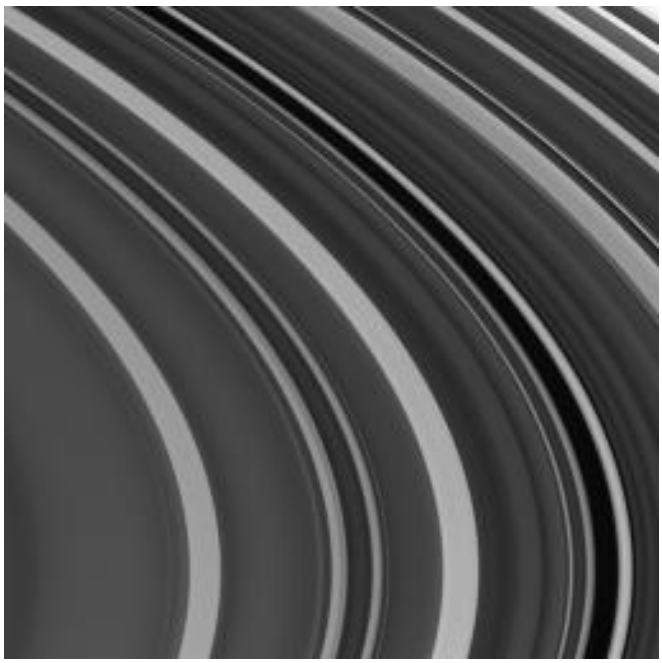

(1d) Plateaus — bright regions unique to the C ring — and gaps are visible in the outer C ring. The dark gap through the center of the image contains the Maxwell Ringlet. The image scale is 4.6 kilometers per pixel.

Figure 1. Images of Saturn's rings captured by Cassini ISS using the narrow angle camera. Image credit: NASA/JPL-Caltech (2004–2017).

ring and the Strange ringlet. We additionally consider the C ring plateaus as their varied dynamical environments are of interest.

Section 2 provides a more detailed overview of RSS occultation observations, and describes the theory of reconstructing optical depth profiles from said observations. Next, in Section 3, we review Mie scattering theory and the relation between particle sizes and differential optical depth measurements. We also illustrate the sensitivity of the radio wavelengths utilized by the Cassini RSS to ring particles ranging from a few millimeters to a few meters in size. In Section 4, we present our results for particle size distributions in the F ring and compare it to particle size distributions in the Strange ringlet and C ring plateaus and to what is known about particle sizes in broader ring regions from investigations which used ultraviolet and infrared wavelengths rather than the longer radio wavelengths used by the Cassini RSS. Our results indicate significant differences between particle sizes in different ring features as well as deviations from standard power law size distributions in certain rings. We suggest possible explanations for these differences based on our data. Finally, in Section 5, we discuss the implications of our results and outline directions for future research, including investigating particle size distributions in other ringlets and embedded ringlets in the C ring and Cassini Division.

2. CASSINI RADIO SCIENCE OBSERVATIONS

The Cassini Radio Science Subsystem (RSS) transmits coherent radiation at wavelengths of 0.94cm (Ka Band), 3.6cm (X Band), and 13cm (S Band) through Saturn's rings in an occultation geometry (Figure 3). The resulting diffraction pattern due to the rings is received by one of NASA's 34m or 70m Deep Space Networks (DSNs) in California, Spain, and Australia, where both the power and phase of incoming radio signals are measured (Asmar et al. 2018). On their own, power measurements are diffraction limited, so we use the difference in phase from the transmitted and incoming radio signals together with the power measurements to reconstruct a profile of the complex transmittance of the rings.

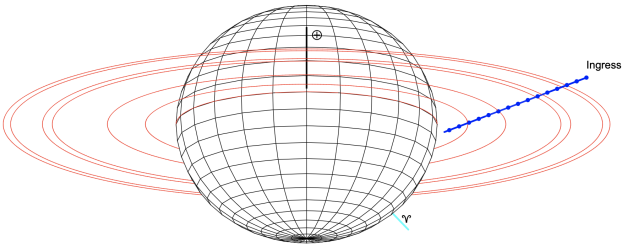

Figure 2. Occultation geometry of Rev 028. The tick marks represent a constant time scale of one hour. The close spacing of tick marks indicates that the occultation was performed slowly from a long distance, which in turn implies a large Fresnel scale for diffraction effects due to the rings. Note how the occultation geometry covers all of the rings in high detail; this indicates that measurements from Rev 028 should have a high signal-to-noise ratio.

2.1. *Occultation Geometry*

The typical geometry of a radio occultation is shown in Figure 3 (see also Marouf et al. (1986), Fig. 1). The coordinate system we use is centered at Saturn; the xy-plane corresponds to the mean surface of the rings, while the z-axis runs through the north pole of Saturn. The unit vector $\hat{\boldsymbol{u}}_{\boldsymbol{i}}$ is directed along the line-of-sight from Earth to Saturn at the time of occultation. Since Cassini and Earth on on opposite sides of the ring, the line-of-sight vector intersects the ring plane at a point which we label $(\rho_0, \phi_0, 0)$, where azimuthal angles are measured with respect to the $x-$axis. $\boldsymbol{R_c}$ is the spacecraft position vector and the distance from the spacecraft to the point on the ring plane where the line of sight intersects is $D = ||\boldsymbol{R_c} - \rho||$. The angle B is the ring opening angle (the elevation angle of Earth above the ring plane).

Note that during the actual Cassini mission, plane waves were transmitted from the spacecraft and received at a DSN on Earth, but in the typical reconstruction method (Marouf et al. (1986)), it is convenient to work with the opposite construction, which yields identical results to the experimental configuration.

2.2. *Theory of Reconstruction*

Marouf et al. (1986) derives the equations to reconstruct the ring profiles by modeling the average effect of ring material on a ray transmitted directly through the rings using the Huygens-Fresnel principle. Consider a plane wave with frequency ω, wavelength λ, and wavenumber $k = \frac{2\pi}{\lambda}$ incident along $\hat{\boldsymbol{u}}_{\boldsymbol{i}}$ on an infinitesimally thin "gray-screen" which represents the ring plane, as in Figure 3. Then, the average complex field E_c observed at $\boldsymbol{R_c}$ can be obtained using wave optics to be approximately

$$E_0 \int\int d\boldsymbol{\rho} \left[\frac{\mu_0}{i\lambda} T(\boldsymbol{\rho}) e^{ik\hat{\boldsymbol{u}}_{\boldsymbol{i}}\cdot\boldsymbol{\rho}}\right] \frac{e^{ik||\boldsymbol{R_c}-\boldsymbol{\rho}||}}{||\boldsymbol{R_c}-\boldsymbol{\rho}||}. \quad (1)$$

where E_0 is a constant, $\mu_0 = \sin B$, and $T(\rho)$ is the function describing the complex transmittance of the rings.

The diffracted complex transmittance, $\hat{T}$, is defined by normalizing the observed signal. Explicitly, we have:

$$\hat{T} = \left(\frac{E_c}{E_0}\right) e^{-ik\hat{\boldsymbol{u}}_{\boldsymbol{i}}\cdot\boldsymbol{R_c}}. \quad (2)$$

Assuming that the rings have circular symmetry over the inversion range, Marouf et al. (1986) combined Eq. 1 and Eq. 2 to obtain:

$$\hat{T}(\rho_0) = \frac{\mu_0}{\lambda}\int_0^\infty \mathrm{d}\rho\rho T(\rho) \int_0^{2\pi} \mathrm{d}\phi \frac{e^{i\psi(\rho_0,\phi_0;\rho,\phi)}}{||\boldsymbol{R_c}-\boldsymbol{\rho}||}, \quad (3)$$

where $\boldsymbol{\rho}_0 = (\rho_0, \phi_0, 0)$ is the point on Saturn's ring plane where the plane wave transmitted from Cassini intersects. ψ is the phase function that accounts for the difference in phase between the transmitted waves and the observed phase. Marouf et al. (1986) use the stationary phase approximation to simplify this equation into a one-dimensional integral equation. In rapidly oscillating integrals, the contributions to the integral come mostly from points of stationary phase, which are points where $\partial\psi/\partial\phi = 0$. If $\phi = \phi_s(\rho, \rho_0, \phi_0, B, D)$ is the solution to $\partial\psi/\partial\phi = 0$, then Eq. 3 approximately reduces to

$$\hat{T}(\rho_0) \approx \frac{1-i}{2F}\int_{-\infty}^{\infty} T(\rho) e^{i\psi(\rho_0,\phi_0;\rho,\phi_s)} \mathrm{d}\rho. \quad (4)$$

where F is the Fresnel scale, given by:

$$F^2 = \frac{\lambda D}{2}\frac{1-\cos^2 B\sin^2\phi_0}{\sin^2 B}, \quad (5)$$

and $D = ||\boldsymbol{R_c} - \boldsymbol{\rho_0}||$, which we assume to be constant.

Previously, Marouf et al. (1986) estimated ψ by iterating the Newton-Raphson method with ϕ_0 as the initial estimate to compute ϕ_s. If $\phi_{s,1}$ is the first-order Newton iterate of ϕ_s, then taking a quadratic Taylor expansion of ψ about $\phi_{s,1}$ yields:

$$\psi \approx \frac{\pi}{2}\left(\frac{\rho-\rho_0}{F}\right)^2. \quad (6)$$

This quadratic approximation produces the Fresnel transform:

$$\hat{T}(\rho_0) = \frac{1-i}{2F}\int_{-\infty}^{\infty} T(\rho) e^{i\frac{\pi}{2}\left(\frac{\rho-\rho_0}{F}\right)^2} \mathrm{d}\rho. \quad (7)$$

which has an explicit inverse given by:

$$T(\rho) = \frac{1+i}{2F}\int_{-\infty}^{\infty} \hat{T}(\rho_0) e^{-i\frac{\pi}{2}\left(\frac{\rho-\rho_0}{F}\right)^2} \mathrm{d}\rho_0, \quad (8)$$

where the integral occurs over the (ρ_0, ϕ_0) plane. That is, we take the complex conjugate of the Fresnel kernel, $\frac{1-i}{2F}e^{i\psi}$, and swap the variable of integration. Mimicing this idea with

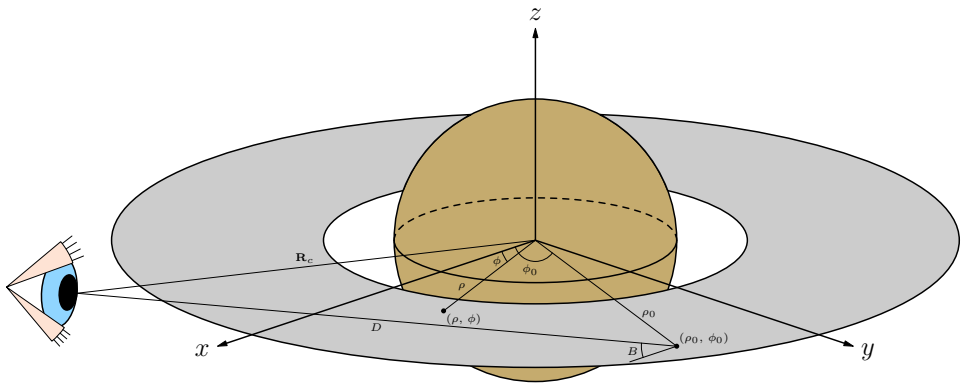

Figure 3. The geometry of an RSS occultation in a Saturnocentric coordinate system. The eye represents Cassini, and $\boldsymbol{R_c}$ is the position vector of Cassini. (ρ_0, ϕ_0) is the point where the line of sight between Cassini and receiver on Earth intersects the ring plane, and $\boldsymbol{\rho} = (\rho, \phi)$ is a dummy variable of integration.

Eqn. 4 gives us the following approximate inverse transform for a general ψ:

$$\tilde{T}(\rho) \approx \frac{1+i}{2F} \int_{-\infty}^{\infty} \hat{T}(\rho_0) e^{-i\psi(\rho_0,\phi_0;\rho,\phi_s)} \mathrm{d}\rho_0. \quad (9)$$

In practice the limits of integration are restricted by the available data and the desired resolution. The window width W is defined in terms of the Fresnel scale F and the resolution R via:

$$W = \frac{2F^2}{R}. \quad (10)$$

Following (Marouf et al. (1986)), the preceding derivation assumes $\hat{\boldsymbol{u}}_{\boldsymbol{i}} \cdot \hat{\boldsymbol{u}}_{\boldsymbol{y}} = 0$, where $\hat{\boldsymbol{u}}_{\boldsymbol{y}}$ is the unit vector along the y axis. The real geometry data available from NASA's Planetary Data System (PDS) show that this dot product is small but not always zero. As the resolution becomes finer, the window width must increase, and the quadratic approximation found in Eqn. 8 becomes insufficient for accurate reconstructions. The higher degree terms needed are more sensitive to the geometry, and the assumption that $\hat{\boldsymbol{u}}_{\boldsymbol{i}} \cdot \hat{\boldsymbol{u}}_{\boldsymbol{y}} = 0$ becomes a source of error for large W (say, a few hundred kilometers or more).

We refine this computation by using the full unsimplified Fresnel phase,

$$\psi = k(\hat{\boldsymbol{u}} \cdot (\boldsymbol{\rho} - \boldsymbol{R}) + ||\boldsymbol{\rho} - \boldsymbol{R_c}||), \quad (11)$$

where $\hat{\boldsymbol{u}}$ is the normalized relative position vector of $\boldsymbol{R_c}$ with respect to $\boldsymbol{\rho} = (\rho, \phi)$, that is:

$$\hat{\boldsymbol{u}} = \frac{\boldsymbol{R_c} - \boldsymbol{\rho}}{||\boldsymbol{R_c} - \boldsymbol{\rho}||}. \quad (12)$$

Moreover, instead of assuming $D = ||\boldsymbol{R_c} - \boldsymbol{\rho_0}||$ is a constant, we calculate it explicitly as a function of Cassini's location relative to Saturn.

This new technique, which we will refer to as the Newton inversion method, allows us to reconstruct the radial structure of the rings at a much higher resolution than before, at up to 100m resolution.

2.3. *Optical Depth and Equivalent Depth*

The normal optical depth, which measures the opacity of the rings, can be related to the complex transmittance, $T(\rho)$ by

$$\tau(\rho) = -2\mu_0 \ln(|T(\rho)|), \quad (13)$$

where $\mu_0 = \sin(B)$ and B is the ring opening angle (Marouf et al. (1986)). In Figure 11 and Figure 12, we present plots of optical depth versus radial distance from Saturn that show the F ring and Strange Ringlet optical depths respectively. The equivalent depth is the radially integrated optical depth.

Noise in the observed data — additive thermal noise introduced primarily at the ground receiving station and multiplicative phase noise

introduced from instability in the oscillators on the spacecraft and at the DSNs — alongside imperfections in the inversion introduce error into the calculation of the normal optical depth and equivalent depth. To limit the effect of noise in our calculations of the equivalent depth of a narrow ringlet, we model the observed ringlet opacity profile using the mathematical shape of a spectral line profile and only select occultations with high signal to noise ratio (SNR). The F ring exhibits noticeable asymmetry in many optical depth profiles (see Figure 11), so rather than using a simple Gaussian or Lorentzian, we model the curves using Ulrik Gelius' asymmetric form (Wertheim (1975)).

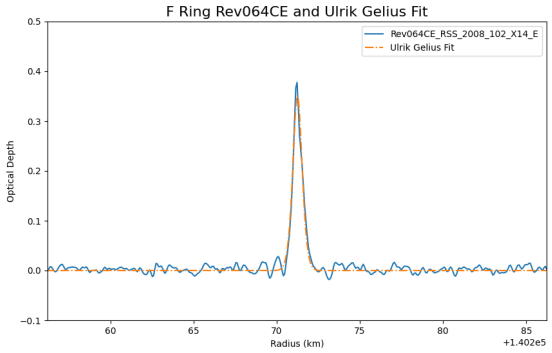

Figure 4. Optical depth profile of the F ring from Rev 064E. Reconstruction was made using the Newton inversion method at 200m and fitted with the asymmetric form due to Ulrik Gelius.

3. MIE SCATTERING THEORY

The optical depth profiles shown in 2.3 are especially useful in estimating particle sizes in Saturn's rings. Each band (Ka, X, and S) can only detect particles comparable in size to its wavelength or larger; as such, comparing data from all three bands allows us to roughly determine how many particles of each size exist. In particular, Mie scattering theory allows us to relate the size distribution of particles in Saturn's rings to the optical depth of the rings themselves. It has been shown that particles in Saturn's rings can be roughly modeled using a truncated power-law size distribution (Dohnanyi (1969)). The number of particles per unit area with radius in the interval $[a, a + da]$, $n(a)$, is given by

$$n(a) = n_0 \left(\frac{a}{a_0}\right)^{-q}, \quad a_{min} \leq a \leq a_{max}, \quad (14)$$

where n_0 is the number of particles per unit area of some arbitrary reference radius a_0, q is the power-law index, and a_{min} and a_{max} are the minimum and maximum particle radii. We assume there are no particles of radius outside the interval $[a_{min}, a_{max}]$. The value of q in Saturn's rings was bounded between 2 and 4 by Dohnanyi (1969), which was improved by Brilliantov et al. (2015) to be between 2.75 and 3.5.

Furthermore, our Mie scattering model assumes that the rings are made up of several layers of discrete spherical particles distributed in accordance to the previously defined power-law. We also neglect multiple scattering effects between layers of a ring. In such a model (also used in Marouf et al. (1983); Jerousek et al. (2020); Cuzzi et al. (2009)), the optical depth τ at a wavelength λ, denoted by $\tau(\lambda)$, is given by

$$\tau(\lambda) = \int_0^\infty \pi a^2 Q_{ext}(a, \lambda) n(a) \mathrm{d}a. \quad (15)$$

Here, we are integrating over all possible particle radii, denoted by a. Also, $Q_{ext}(a, \lambda)$ is the extinction (scattering plus absorption) efficiency of a particle of radius a due to radiation (light) of wavelength λ. More specifically, $Q_{ext}(a, \lambda) = \frac{\sigma_{ext}(a,\lambda)}{\pi a^2}$, where σ_{ext} is the cross section of extinction of a particle. The dependence of Q_{ext} on wavelength at various particle sizes is pictured in Figure 5a.

3.1. *Constraining the Size Distribution*

Though we have shown it is possible to determine the differential opacity given the par-

ticle size distribution, our goal is to infer the size distribution from the opacity measurements themselves. Marouf et al. (1983) show that this can be accomplished via the differential opacity measurement $\Delta\tau(\lambda_1, \lambda_2) = \tau(\lambda_1) - \tau(\lambda_2)$. Defining $Q_\Delta(a, \lambda_1, \lambda_2) = Q_{ext}(a, \lambda_1) - Q_{ext}(a, \lambda_2)$, and given the power-law index q and a_{max}, it is possible to invert Eq. 15 to recover the following expression for $n(a_0)$:

$$\frac{\Delta\tau(\lambda_1, \lambda_2)}{\int_{a_{min}}^{a_{max}} \pi a^2 Q_\Delta(a, \lambda_1, \lambda_2) \left(\frac{a}{a_0}\right)^{-q} \mathrm{d}a}. \quad (16)$$

Given this, it only remains to determine q, a_{min}, and a_{max} in order to entirely determine the power-law size distribution of particles in Saturn's rings. Figure 5b shows that values of q and a_{max} uniquely determine normalized differential opacity $\frac{\Delta\tau(X,S)}{\tau(X)}$. The same is true for $\frac{\Delta\tau(K,X)}{\tau(K)}$; as such, we are able to significantly constrain q, a_{min}, and a_{max} by plotting $\frac{\Delta\tau(K,X)}{\tau(K)}$ and $\frac{\Delta\tau(X,S)}{\tau(X)}$ against each other. This is shown in Figure 6. Another method of determining the distribution $n(a)$ is by comparing the values of $\frac{\Delta\tau(KX)}{\tau(X)}$ and $\frac{\Delta\tau(XS)}{\tau(X)}$ by plotting them against each other as shown in Figure 6. Of note are the small particles (around 1 millimeter) which make up the "tail" on the right side of the curves in Figure 6; as particles get to this size range, the value of a is so small compared to the wavelengths of the Ka, X, and S bands that the differential opacity remains relatively constant. As such, for each q value, these graphs saturate at some point on their tails and do not change even if a_{min} is decreased.

Additionally, particles much larger than the Ka, X, and S bands (around 1 meter in radius) end up at the origin of the differential opacity graph as almost no diffraction pattern is formed by radiation hitting a "wall" much larger than its wavelength.

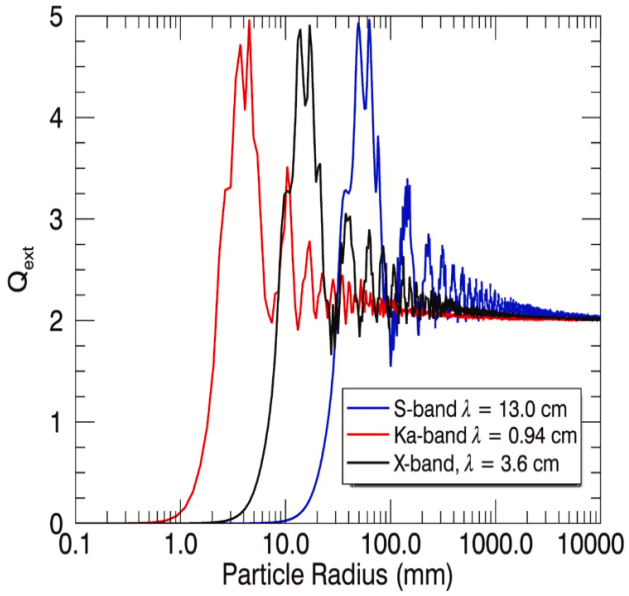

(5a) Extinction efficiency versus particle radius for the Ka band, X band, and S band, derived from Mie theory. All three curves approach 2 as particle radius increases due to Babinet's principle (Jerousek et al. (2020)).

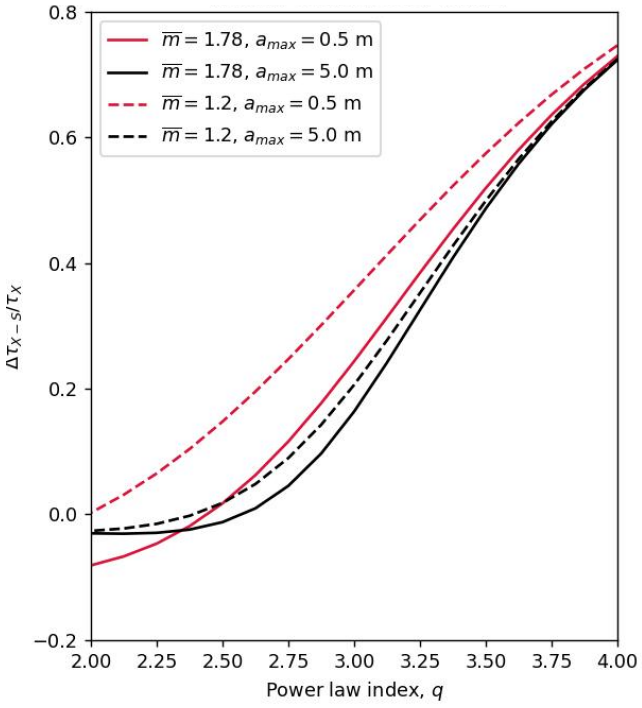

(5b) Normalized differential opacity $\frac{\Delta\tau(XS)}{\tau(X)}$ plotted against power-law index q from Marouf et al. (1983). Each curve is monotonically increasing with q and shows that a given measurement of $\frac{\Delta\tau(KX)}{\tau(X)}$ along with the value of a_{max} correspond to a unique value of q.

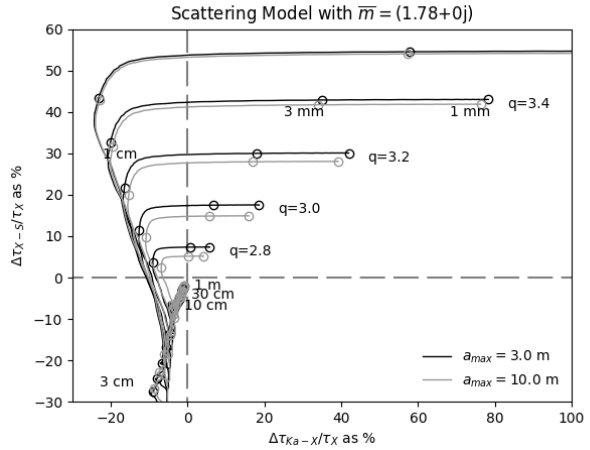

Figure 6. A differential opacity curve plotting normalized differential opacities $\frac{\Delta\tau(XS)}{\tau(X)}$ versus $\frac{\Delta\tau(KX)}{\tau(X)}$. Model curves for power-law indices from 2.8 to 3.6 in increments of 0.2 and a_{max} values of 3m and 10m are shown. Also, a_{min} ranges from 1mm to 1m for each curve.

4. RESULTS

4.1. *The F Ring*

Due to its discontinuous nature, the F ring is only convincingly detected in about $\frac{1}{3}$ of Cassini occultations (Cuzzi et al. (2024)). Of these occultations, we identified the few with the highest SNR, fitted them with the asymmetric form due to Ulrik Gelius (see Figure 4), and integrated the profiles to find the equivalent depths. Then, we plotted the differential $\Delta\tau(KX)$ and $\Delta\tau(XS)$ opacities overlaid on several differential opacity model curves (Figure 7).

Assuming a_{max} = 10m, we calculated the best fit values a_{min} and q for each occultation and averaged them (see Table 1). The power law index we found for the F ring (3.34) was significantly higher than the known values for other ring regions and the a_{min} value of 1.42mm was significantly lower than known values, suggesting the F ring particle size distribution contains significantly more small particles than other ring regions. Note that a key feature of F ring differential opacity measurements is their high normalized $\Delta\tau(KX)$ values. In particular, these

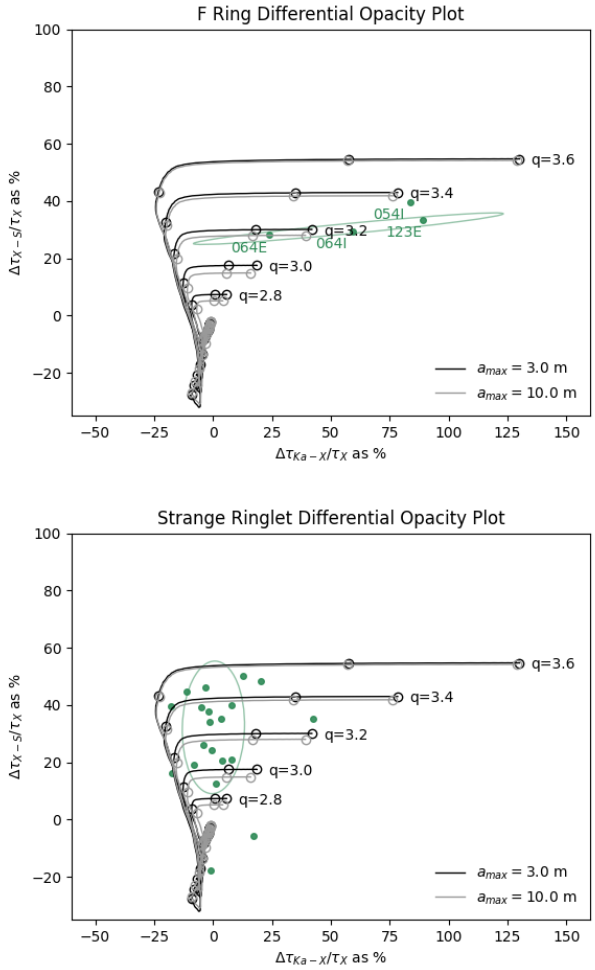

Figure 7. Normalized optical depth values plotted with model curves in the F ring and Strange ringlet. The ellipse indicates a 2 standard deviation confidence interval around the mean.

values for Revs 064I, 054I, 123E, and others, are larger than the maximum possible values indicated by the model curves. Thus, the best fit power-law values for the F ring have larger error values than we see in other ring features. This indicates that particle size distributions in the F ring do not follow a standard power-law size distribution as previously assumed. We explore possible explanations to this phenomenon in Section 5.

4.2. *The Strange Ringlet*

Another narrow ringlet of interest to us is the Strange ringlet. Also known as R6, the Strange

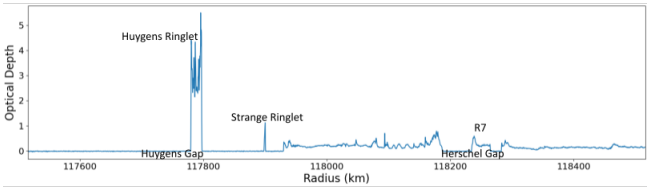

Figure 8. Occultation profile of a portion of the Cassini Division, including the Strange ringlet and its surroundings. This profile was created from the Cassini RSS Rev007 Ingress occultation, using the X43 band and Newton psitype, as described in Section 2.

ringlet resides in the Huygens Gap, which separates the B ring from the Cassini Division proper (see Figure 8). The ringlet was first detected in the Voyager photo-polarimeter system (PPS) (Colwell et al. (2009)) and is seen clearly in many Cassini images and occultations. The Strange ringlet receives its name from its significant incline with respect to the main ring plane, which causes it to sometimes appear to leave the Huygens Gap and appear superimposed in the region outside the Huygens Gap. It is almost opaque in some occultations — which may explain its absence in Voyager occultations — and is only a few kilometers wide (Colwell et al. (2009)).

The Strange ringlet is similar to the F ring in many ways — both are narrow, elliptical, and inclined rings and they have very similar widths (both are around 3km wide). Thus, it seems natural to compare the particle size distributions of the F ring and the Strange ringlet to determine whether the particle size distribution of the F ring is truly unique because of its chaotic environment and clumpy nature. A few high SNR profiles of the Strange ringlet at 200m resolution are shown in Figure 12.

Figure 7 compares the particle size distributions of the F ring and the Strange ringlet. Note that the size distribution of the Strange ringlet shows significantly more vertical spread than the F ring, but has a rather small horizontal spread with majority of the occultations showing differential KX values close to 0. This indicates that the Strange ringlet has larger particles on average than the F ring, which is backed up by our calculated values of a_{min} and q (see Table 1). The Strange ringlet size distribution is closer to the calculated values of other regions, suggesting the particle size distribution in the F ring is unique.

4.3. *C Ring Plateaus*

The C ring plateaus are optically "bright" regions which wary from about 40km to about 250km in width (see Figure 1d). A total of 11 plateaus have been identified, but their origin remains unknown (Colwell et al. (2009)). The optical depth at the center of each C ring plateau is several times that of the surrounding area, but the plateau's optical depths are highest in the edges, giving them a U-shaped profile (see Figure 10). Hedman & Nicholson (2014) find that the large optical depth difference between the plateaus and the C ring background are either due to differences in particle size distribution or in particle densities. We study the particle sizes within this plateaus to investigate similarities and differences within the 11 plateaus and to compare particle size distribution within the plateaus to those of narrow ringlets like the Strange ringlet and F ring.

Using the radial bounds for the plateaus identified by Colwell et al. (2009), we calculated the equivalent depth by numerically integrating the optical depth profiles within these radial bounds, then calculated the differential $\Delta\tau(KX)$ and differential $\Delta\tau(XS)$ opacities and plotted them in Fig 9. Note that the reconstructed profiles of the plateaus were much nosier for later occultations with low ring opening angles (see Fig 10). Thus, to ensure accuracy in our data, we included only occultations with a ring opening angle above 14 degrees.

Our results suggest that the plateaus vary significantly from one another in differential $\Delta\tau(XS)$ opacity, but seemed to consistently all

have close to zero differential $\Delta\tau(KX)$ opacity. We determined the best fit a_{min} and q values for each plateau, shown in Table 1.

Jerousek et al. (2020) conducted a similar analysis of particle sizes on the C ring plateaus using data from stellar occultation from the Cassini Ultraviolet Imaging Spectrograph (UVIS) and the Visual and Infrared Mapping Spectrometer (VIMS), as well as one occultation (Rev 007) from the RSS. UVIS and VIMS measured at wavelengths 0.15µm and 2.92µm respectively, so they detected much smaller particles than the RSS data. Notably, our data showed more variation among the plateaus than Jerousek et al. (2020). For example, while P6 was the plateau with the highest q mean of all plateaus in both data sets, Jerousek et al. (2020) found a q mean of 3.21 while our calculated q mean was 3.41. One possible explanation for the difference is that the RSS data is more sensitive to larger particles because it spans wavelengths of 0.94cm, 3.6cm, and 13cm, which is significantly larger than the wavelengths of UVIS and VIMS. We explore methods of consolidating our results with those of Jerousek et al. (2020) in Section 5.

Feature	q Mean	q SD	a_{min} Mean (mm)	a_{min} SD (mm)
F ring	3.34	0.12	1.42	0.72
Strange ringlet	3.25	0.17	5.49	207.69
P1	3.16	0.09	4.21	1.02
P2	3.19	0.08	4.74	0.40
P3	3.15	0.09	4.31	0.70
P4	3.31	0.04	4.63	0.22
P5	3.00	0.01	3.89	0.34
P6	3.41	0.04	4.75	0.22
P7	3.05	0.02	4.09	3.05
P8	3.17	0.04	4.28	0.88
P9	3.18	0.03	4.30	0.26
P10	3.19	0.03	4.31	0.27
P11	2.76	0.04	64.89	241.45

Table 1. Mean and standard deviation (SD) of best fit q and a_{min} values over various ring features. a_{max} is assumed to be 10m.

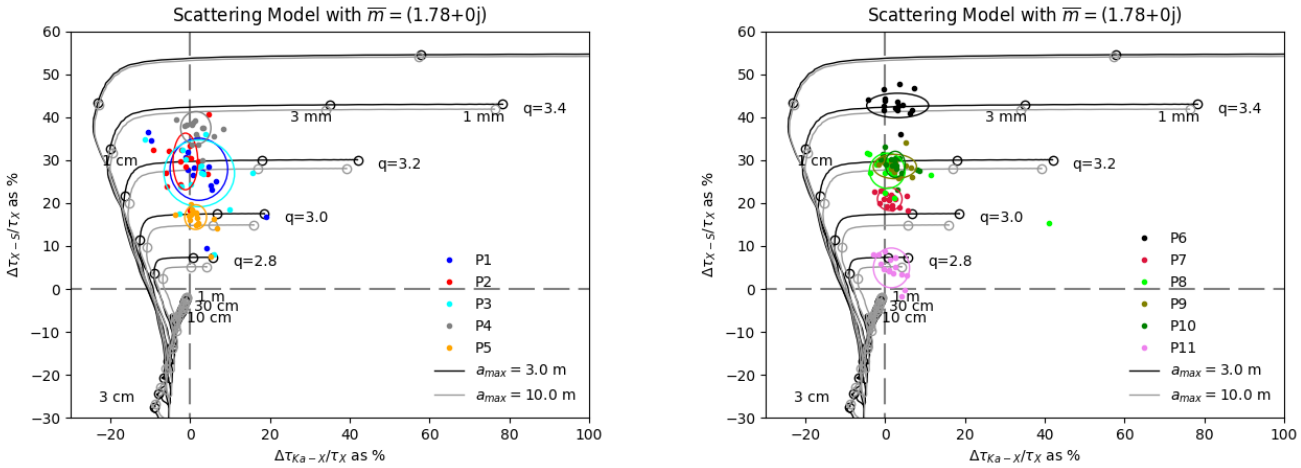

Figure 9. 2D differential opacity plot of C ring plateaus $1-5$ (left) and plateaus $6-11$ (right). Differential opacities were obtained over all RSS occultations with ring opening angle over 14 degrees. Underlaid are differential opacity curves with power laws $q = 2.8, 3.0, 3.2, 3.4$. Points $a_{min} = 0.1, 0.3, 1, 3, 10, 30$ and 100cm are identified.

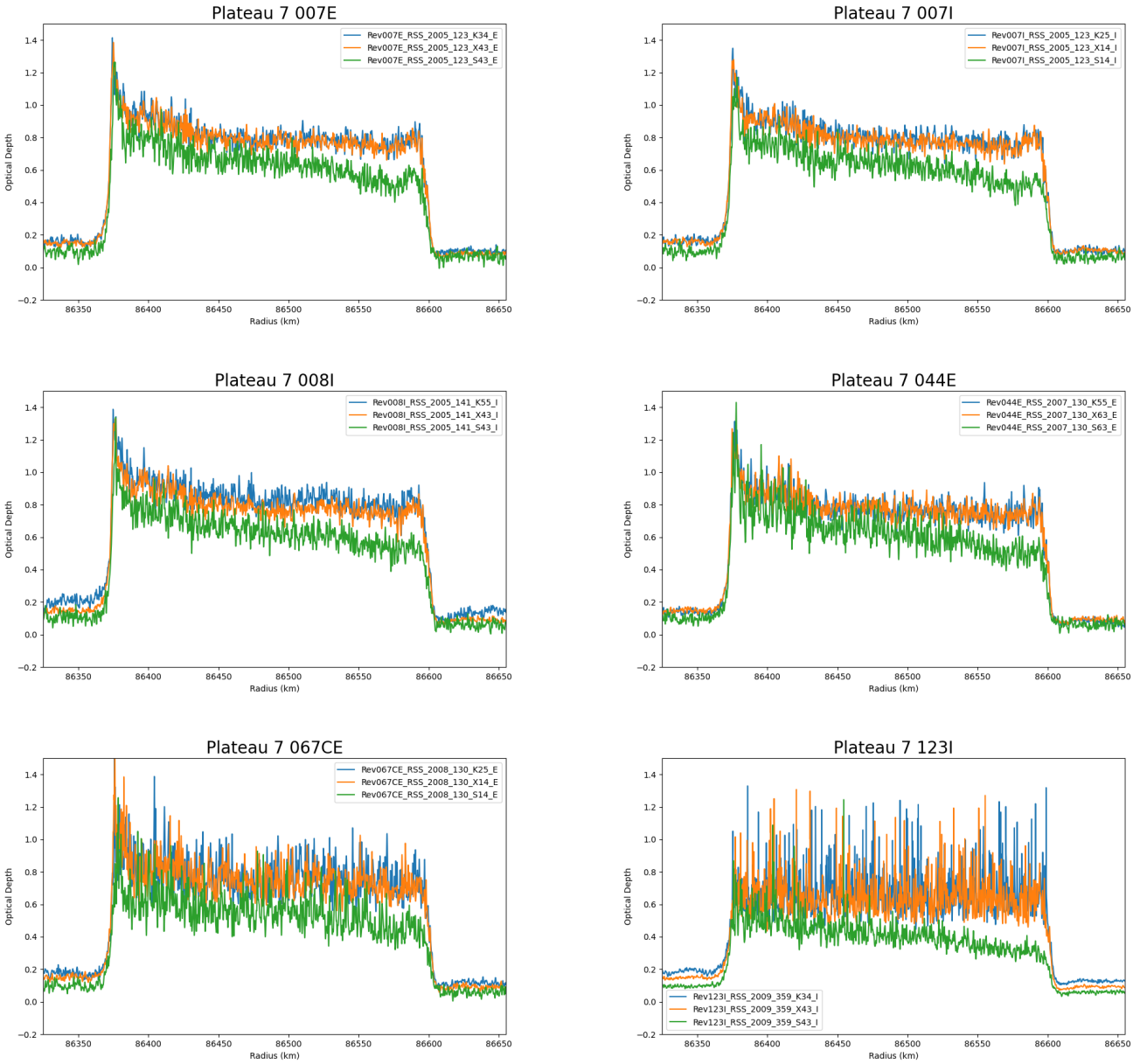

Figure 10. Optical depth profiles for Plateau 7 across a selection of occultations. Reconstructions were retrieved using the Newton inversion method at 500m resolution. Note that the SNR of the early occultations (Revs 007E, 007I, and 008I) is much higher than the SNR of the late occultations (Revs 067E and 123I).

5. DISCUSSION

Our survey of the F ring, Strange ringlet, and C ring plateaus reveals substantial regional differences in differential opacity at the Ka, X, and S radio wavelengths. The simplest explanation for these differences is a difference in the particle size distributions between these regions. Since ring particles are icy aggregates that fragment and coalesce with interparticle collisions, the particle sizes are reflections of the dynamical environment of each region.

Another possible explanation for the difference between our calculated F ring particle size

distribution and known values for other regions is the clumpiness of the F ring observed by Esposito et al. (2008) and Alrebdi & Esposito (2025). Since the reconstruction method assumes radial symmetry of the rings across the processing window, the presence of kittens in the F ring may effect the accuracy of the reconstruction. We plan to investigate whether the purported clumpiness of the F ring can inferred from the differential opacity measurements from the RSS observations. We also plan to investigate particle size distributions of other ringlets and embedded ringlets within the C ring and Cassini division and compare them to our observations in the Strange ringlet and F ring. Finally, to consolidate our findings of the particle size distributions in the C ring plateaus with the findings in Jerousek et al. (2020), we will compare the C ring plateau particle size differences with regional differences in textures in the rings observed in Cassini images.

APPENDIX

A. RSS OCCULTATION PROFILES

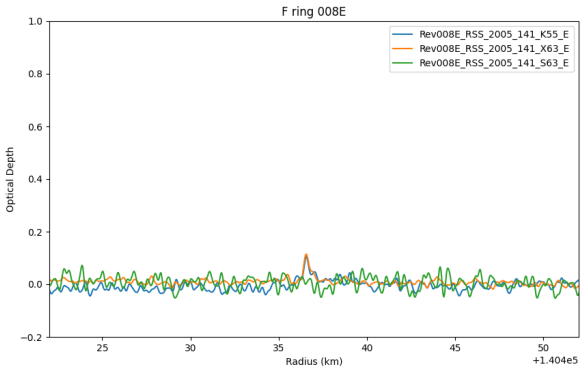

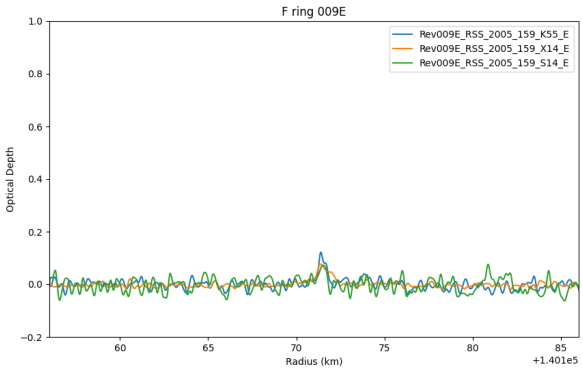

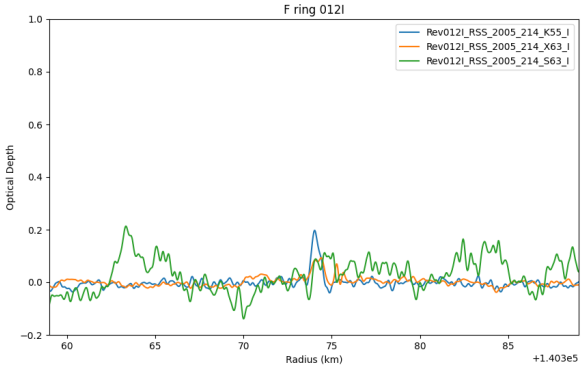

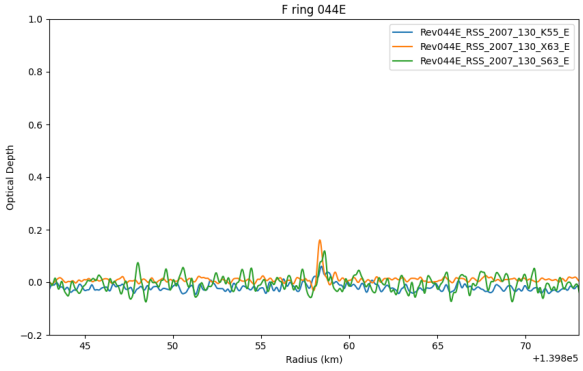

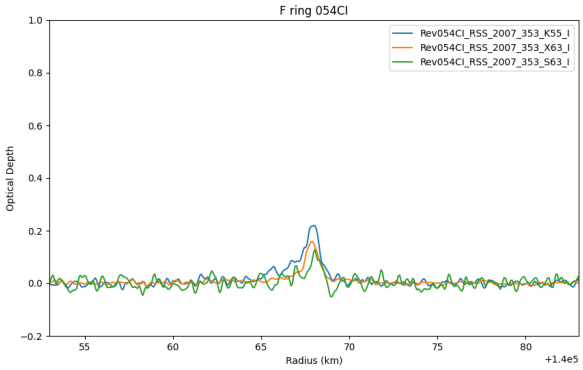
F ring 054CI
Rev054CI_RSS_2007_353_K55_I
Rev054CI_RSS_2007_353_X63_I
Rev054CI_RSS_2007_353_S63_I
Optical Depth
Radius (km)
+1.4e5

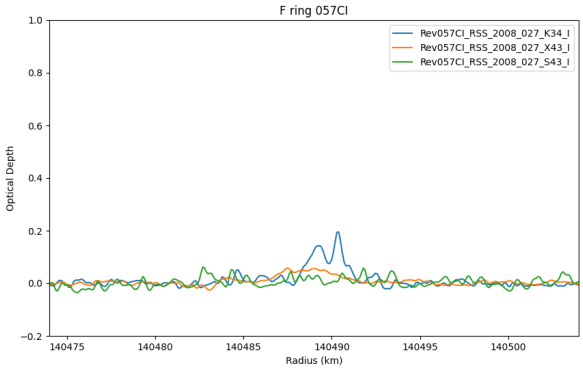
F ring 057CI
Rev057CI_RSS_2008_027_K34_I
Rev057CI_RSS_2008_027_X43_I
Rev057CI_RSS_2008_027_S43_I
Optical Depth
Radius (km)

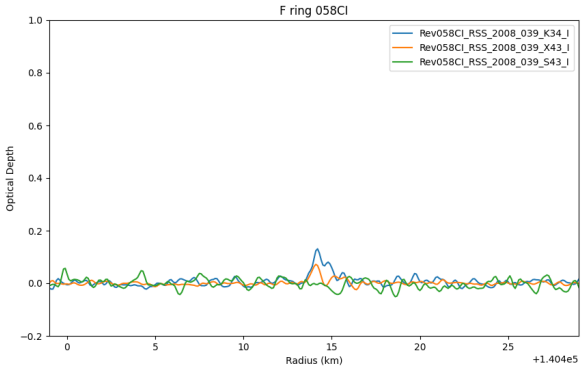
F ring 058CI
Rev058CI_RSS_2008_039_K34_I
Rev058CI_RSS_2008_039_X43_I
Rev058CI_RSS_2008_039_S43_I
Optical Depth
Radius (km)
+1.404e5

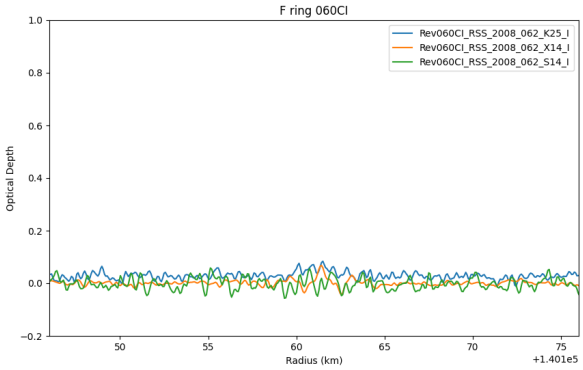
F ring 060CI
Rev060CI_RSS_2008_062_K25_I
Rev060CI_RSS_2008_062_X14_I
Rev060CI_RSS_2008_062_S14_I
Optical Depth
Radius (km)
+1.401e5

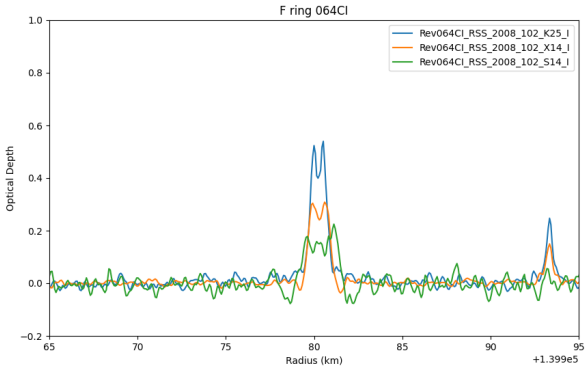
F ring 064CI
Rev064CI_RSS_2008_102_K25_I
Rev064CI_RSS_2008_102_X14_I
Rev064CI_RSS_2008_102_S14_I
Optical Depth
Radius (km)
+1.399e5

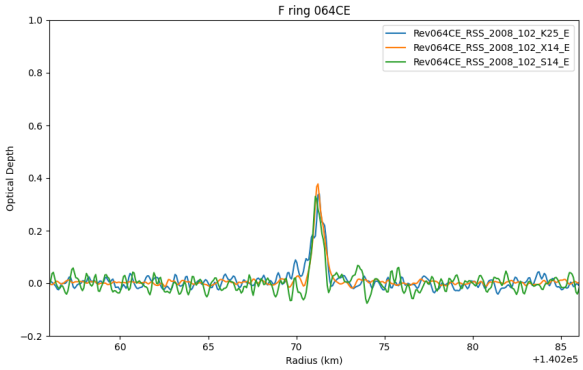
F ring 064CE
Rev064CE_RSS_2008_102_K25_E
Rev064CE_RSS_2008_102_X14_E
Rev064CE_RSS_2008_102_S14_E
Optical Depth
Radius (km)
+1.402e5

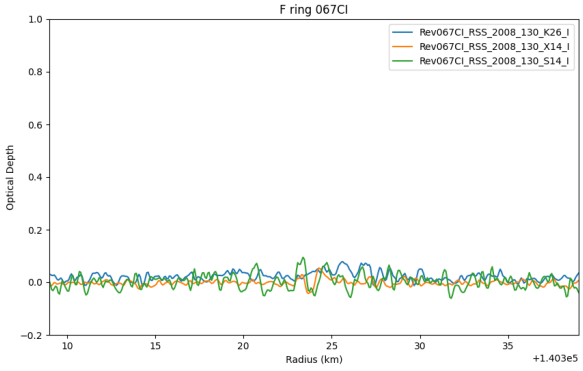
F ring 067CI
Rev067CI_RSS_2008_130_K26_I
Rev067CI_RSS_2008_130_X14_I
Rev067CI_RSS_2008_130_S14_I
Optical Depth
Radius (km)
+1.403e5

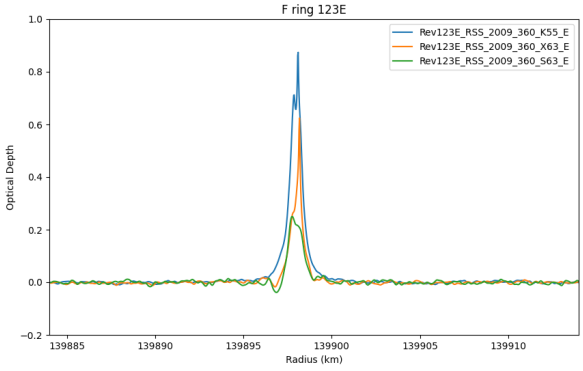
F ring 123E
Rev123E_RSS_2009_360_K55_E
Rev123E_RSS_2009_360_X63_E
Rev123E_RSS_2009_360_S63_E
Optical Depth
Radius (km)

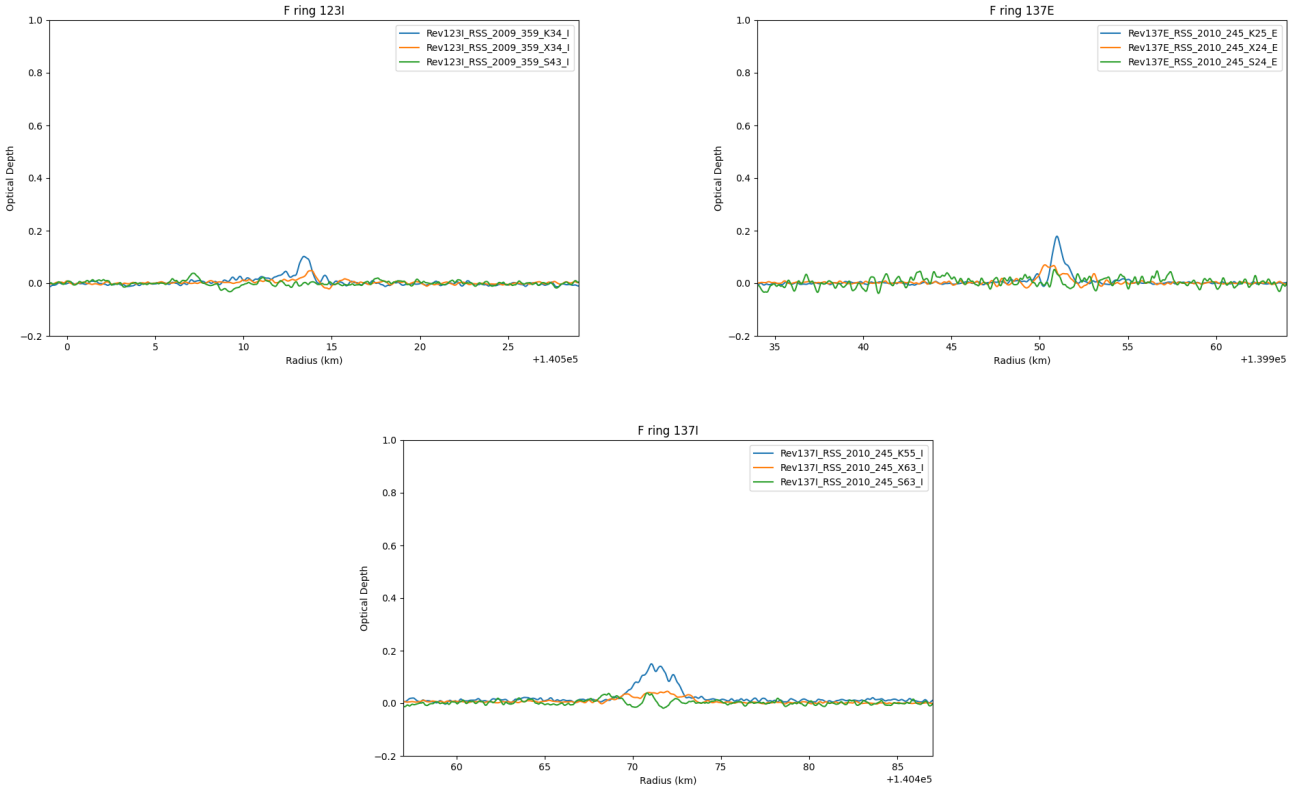

Figure 11. Gallery of normalized optical depth profiles on three wavelengths (Ka, X, and S band) across all 15 F ring detections before ultra-stable oscillator (USO) failure. These profiles were obtained using the Newton inversion method, and are all at 200m resolution, except Rev057I and Rev058I, which are at 300m resolution. The vertical scale ranges from −0.2 to 1. Note that some occultations have much higher optical depth than others; in particular, we identified Revs 054I, 64I, 64E, and 123E as having clear detections with high SNR.

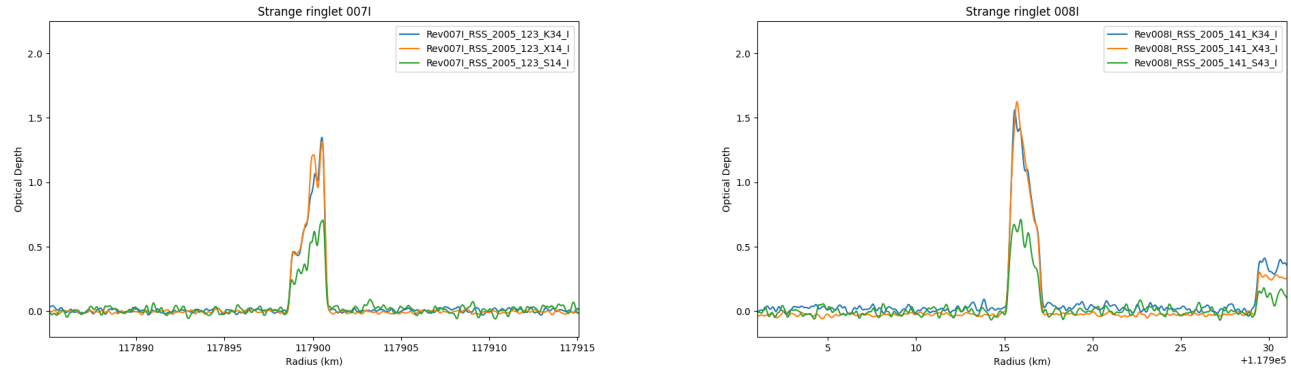

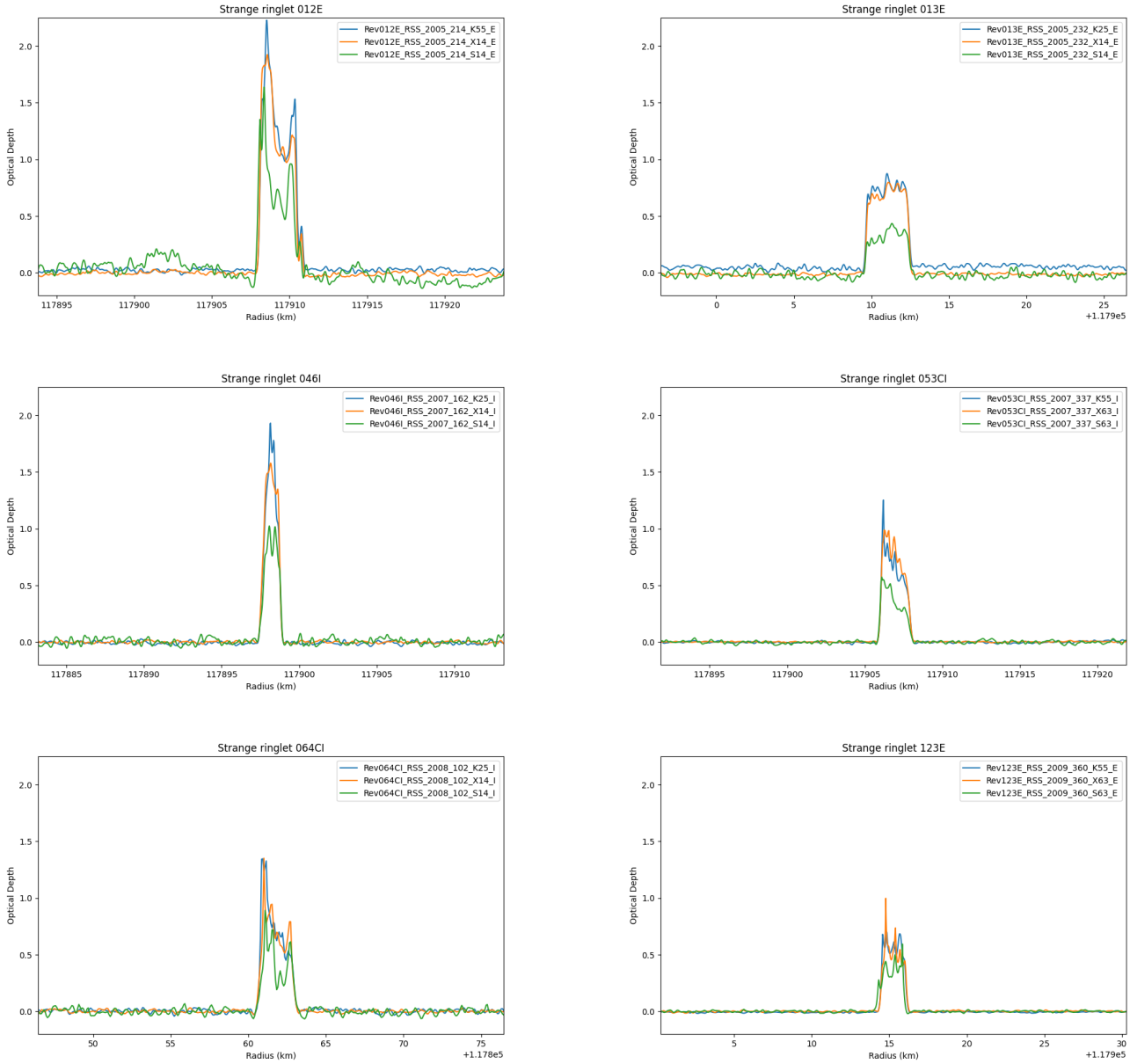

Figure 12. Gallery of normalized optical depth profiles of the Strange ringlet on three wavelengths (Ka, X, and S band) across a representative selection of occultations. These profiles were obtained using the Newton inversion method, and are all at 200m resolution. The vertical scale (the normalized optical depth) ranges from -0.2 to 2.25.

REFERENCES

Alrebdi, A., & Esposito, L. W. 2025, Icarus, 441, 116709, doi: https://doi.org/10.1016/j.icarus.2025.116709

Asmar, S. W., French, R. G., Marouf, E. A., et al. 2018, Cassini Radio Science User's Guide, 1st edn., NASA Jet Propulsion Laboratory

Brilliantov, N., Krapivsky, P. L., Bodrova, A., et al. 2015, Proceedings of the National Academy of Sciences, 112, 9536, doi: 10.1073/pnas.1503957112

Colwell, J. E., Nicholson, P. D., Tiscareno, M. S., et al. 2009, The Structure of Saturn's Rings, ed. M. K. Dougherty, L. W. Esposito, & S. M. Krimigis (Dordrecht: Springer Netherlands), 375–412, doi: 10.1007/978-1-4020-9217-6_13

Cuzzi, J., Clark, R., Filacchione, G., et al. 2009, in Saturn from Cassini-Huygens, ed. M. K. Dougherty, L. W. Esposito, & S. M. Krimigis (Dordrecht: Springer Netherlands), 459–509, doi: 10.1007/978-1-4020-9217-6_15

Cuzzi, J. N., Marouf, E. A., French, R. G., Murray, C. D., & Cooper, N. J. 2024, Science Advances, 10, eadl6601, doi: 10.1126/sciadv.adl6601

Dohnanyi, J. S. 1969, Journal of Geophysical Research (1896-1977), 74, 2531, doi: https://doi.org/10.1029/JB074i010p02531

Esposito, L. W., Meinke, B. K., Colwell, J. E., Nicholson, P. D., & Hedman, M. M. 2008, Icarus, 194, 278, doi: https://doi.org/10.1016/j.icarus.2007.10.001

Hedman, M. M., & Nicholson, P. D. 2014, Monthly Notices of the Royal Astronomical Society, 444, 1369, doi: 10.1093/mnras/stu1503

Jerousek, R. G., Colwell, J. E., Hedman, M. M., et al. 2020, Icarus, 344, 113565, doi: 10.1016/j.icarus.2019.113565

Marouf, E. A., Leonard Tyler, G., Zebker, H. A., Simpson, R. A., & Eshleman, V. R. 1983, Icarus, 54, 189, doi: 10.1016/0019-1035(83)90192-6

Marouf, E. A., Tyler, G. L., & Rosen, P. A. 1986, Icarus, 68, 120

Murray, C. D., & French, R. S. 2018, The F Ring of Saturn, ed. M. S. Tiscareno & C. D. Murray, Cambridge Planetary Science (Cambridge University Press), 338–362

NASA/JPL-Caltech. 2004–2017, NASA/JPL Photojournal, https://photojournal.jpl.nasa.gov/

Wertheim, G. 1975, Journal of Electron Spectroscopy and Related Phenomena, 6, 239, doi: https://doi.org/10.1016/0368-2048(75)80019-3